Colloidal Bimetallic RuNi Particles and their Behaviour in Catalytic Quinoline Hydrogenation

Miquel Cardona-Farreny, Hiroya Ishikawa, Abolanle Olatilewa Odufejo Ogoe, Sonia Mallet-Ladeira, Yannick Coppel, Pierre Lecante, Jerome Esvan, Karine Philippot, M. Rosa Axet

Research Article
doi.org/10.1002/cplu.202400516

Chemistry Europe
European Chemical Societies Publishing

www.chempluschem.org

Colloidal Bimetallic RuNi Particles and their Behaviour in Catalytic Quinoline Hydrogenation

Miquel Cardona-Farreny,[a] Hiroya Ishikawa,[a] Abolanle Olatilewa Odufejo Ogoe,[a] Sonia Mallet-Ladeira,[a, b] Yannick Coppel,[a] Pierre Lecante,[c] Jerome Esvan,[d] Karine Philippot,[a] and M. Rosa Axet*[a]

Colloidal metal nanoparticles exhibit interesting catalytic properties for the hydrogenation of (hetero)arenes. Catalysts based on precious metals, such as Ru and Rh, promote this reaction efficiently under mild reaction conditions. In contrast, heterogeneous catalysts based on earth-abundant metals can selectively hydrogenate (hetero)arenes but require harsher reaction conditions. Bimetallic catalysts that combine precious and earth-abundant metals are interesting materials to mitigate the drawbacks of each component. To this end, RuNi nanoparticles bearing a phosphine ligand were prepared through the decomposition of $[Ru(\eta^4\text{-}C_8H_{12})(\eta^6\text{-}C_8H_{10})]$ and $[Ni(\eta^4\text{-}C_8H_{12})_2]$ by H_2 at 85 °C. Wide angle X-ray scattering confirmed a bimetallic segregated structure, with Ni predominantly on the surface. Spectroscopic analyses revealed that the phosphine ligand coordinated to the surface of both metals, suggesting, as well, a partial Ni shell covering the Ru core. The RuNi-based nanomaterials were used as catalysts in the hydrogenation of quinoline to assess the impact of the metallic composition and of the stabilizing agent on their catalytic performance.

Introduction

Transition-metal catalysis has had an enormous impact in chemical synthesis, both in academia and industry. Nevertheless, these applications rely mainly on precious metals. The low natural abundance of these elements, their cost in terms of environmental impact, price, and/or geopolitical risks push to explore materials based on earth-abundant metals for numerous applications, including catalysis.[1,2] Increasingly efforts are devoted to the use of earth-abundant metals in homogeneous catalysis, but much remains to be explored in heterogeneous catalysis. Given that earth-abundant metals have distinct electronic structure, thermochemistry, and kinetics compared to precious metals, that have consequences in their activity, selectivity, and robustness, alternative strategies need to be developed for their implementation as catalysts. A similar scenario is found specifically for the hydrogenation of (hetero)arenes. In the past, much effort has been invested in developing homogeneous and heterogeneous catalysts based on precious metals,[3,4] but the focus is now shifting towards providing hydrogenation catalysts based on earth-abundant metals.[5] In recent years, examples of the use of heterogeneous catalysts based on earth-abundant metals for the hydrogenation of (hetero)arenes have been flourishing, including Ni,[6–8] Co,[9–14] Cu,[15,16] and Fe.[17] Nevertheless, in general, harsher reaction conditions are needed compared to precious metal-based catalysts,[18–20] limiting their applications and compromising their robustness. Usually, temperatures and pressures ranging from 100 to 160 °C and from 2 to 6 MPa are needed[21]; with only a few recent examples demonstrating the ability to proceed under milder reaction conditions.[6,8,12–14] A straightforward strategy to increase the robustness and catalytic performance of earth-abundant metal-based catalysts is to associate them with another metal[22] or p-block atom.[23] For the hydrogenation of (hetero)arenes, Ni-based catalysts have been combined with Ir,[24] Si[25] or La[26] or used in trimetallic systems such as FeNiCu,[27] resulting in increased activity or robustness. For instance, Nilr/SiO_2 displayed a synergetic effect between both metals.[24] We have recently observed a synergetic effect between metals on activity in a RuNi colloidal catalysts for the hydrogenation of furfural, with an optimum ratio of Ru:Ni 1:1.[22] Taking into consideration the high efficiency of Ru-based catalysts for the hydrogenation of (hetero)arenes,[3,21] and based on our findings described above, we hypothesised that a RuNi based catalyst could be of interest for the hydrogenation of (hetero)arenes. Thus, in this work, two sorts of RuNi based catalysts have been successfully synthesised, and then tested for the hydrogenation of quinoline, and compared to their

[a] M. Cardona-Farreny, H. Ishikawa, A. O. Odufejo Ogoe, S. Mallet-Ladeira, Y. Coppel, K. Philippot, M. R. Axet
CNRS, LCC (Laboratoire de Chimie de Coordination), Université de Toulouse, UPS, INPT, 205 route de Narbonne, BP 44099, F-31077 Toulouse Cedex 4, France
E-mail: rosa.axet@lcc-toulouse.fr

[b] S. Mallet-Ladeira
Institut de Chimie de Toulouse (UAR 2599), 31062 Toulouse Cedex 09, France

[c] P. Lecante
Centre d'élaboration des matériaux et d'études structurales UPR CNRS 8011, 29 Rue Jeanne-Marvig, BP 4347, 31055 Toulouse, France

[d] J. Esvan
CIRIMAT, Université de Toulouse, CNRS-INPT-UPS, 4 Allée Emile Monso, BP 44362, 31030 Toulouse, France

Supporting information for this article is available on the WWW under https://doi.org/10.1002/cplu.202400516

respective monometallic counterparts. In one hand, our previous described RuNi colloidal nanoparticles (NPs) stabilized with polyvinylpyrrolidone (PVP),[22] and a second RuNi unsupported catalyst stabilized with a phosphine ligand, diphenyl-2-pyridylphosphine, PPh_2Py. The choice of the catalytic materials lies in the aim of improving an earth-abundant metal-based catalyst for the hydrogenation of (hetero)arenes. First, by alloying it with a precious metal, which is expected to provide robustness and higher catalytic activity. Additionally, the presence of the more electropositive metal, Ni, should increase the electron density of Ru, which usually enhances reaction rates. Second, coordinating a donor ligand should increase robustness of the material by forming a strong bond with the surface, while also contributing additional electronic density to the surface.

Experimental Section

General Methods. All operations were carried out under argon atmosphere using standard Schlenk techniques or in a glovebox. Solvents were purified by standard methods or by an MBraun SPS-800 solvent purification system. $[Ru(\eta^4\text{-}C_8H_{12})(\eta^6\text{-}C_8H_{10})]$ was purchased from Nanomeps Toulouse, $[Ni(\eta^4\text{-}C_8H_{12})_2]$ from Strem Chemicals, PPh_2Py, quinoline, 1,2,3,4-tetrahydroquinoline (1-THQ), 5,6,7,8-tetrahydroquinoline (5-THQ) and decahydroquinoline (DHQ) from TCI, solvents and PVP from Aldrich, H_2 from Air Liquid. All these reactants were used as received. Metal content was established by inductively coupled plasma optical emission spectroscopy (ICP-OES) performed at the "Laboratoire de Chimie de Coordination, Toulouse" in a Thermo Scientific ICAP 6300 instrument. Liquid NMR measurements were performed on a Bruker Avance 300 or 400 instrument. Solid-state NMR experiments were recorded on a Bruker Avance 400 III HD spectrometer. Samples were packed into 3.2 mm zirconia rotors under argon inside a glovebox. The rotors were rotated at frequencies between 15 and 26 kHz at 295 K. ^1H MAS were performed with the DEPTH pulse sequence and a recycle delay of 3 s. Ramped cross-polarization (CP) $^1H\rightarrow{}^{13}C$ MAS spectra were recorded with a recycle delay of 1.5 s and a contact time of 2 ms. ^{31}P Hahn-echo were recorded with a recycle time of 10 s and an echo time of 1 rotor period. To highlight signals affected by Knight-shift, variable offset cumulative spectra (VOCS)[28] of ^{31}P Hahn-echo were recorded with a recycle time of 0.1 s. All the ^{13}C and ^{31}P-NMR spectra were recorded under high-power proton decoupling conditions. Chemical shifts were referenced to TMS, and 85% H_3PO_4 for ^1H, ^{13}C and ^{31}P, respectively. Attenuated total reflection infrared (ATR-IR) spectra were recorded on a Perkin-Elmer GX2000 spectrometer available in a glovebox, in the range 4000–400 cm^{-1} Transmission electron microscopy (TEM) analyses were performed at the "Centre de microcaracterisation Raimond Castaing, UMS 3623, Toulouse" by using a JEOL JEM 1400 operating at 120 kV with a point resolution of 2.0 Å. The approximation of the particles mean size was established through a manual analysis of enlarged micrographs by measuring at least 200 particles on a given grid for as-synthesised nanomaterials, or 50 for the samples after catalysis. The magnetic hysteresis curves were acquired by using a MPMS 5 QUANTUM DESIGN Magnetometer (cryo-aimant 5T; cryostat 2 K–400 K) using a superconducting quantum interference device (SQUID). Wide angle X-ray scattering (WAXS) measurements were performed at CEMES on a diffractometer dedicated to pair distribution function (PDF) analysis: graphite-monochromatized molybdenum radiation (0.07169 nm), solid-state detection and low background setup. Samples were sealed in Lindemann glass capillaries (diameter 1 mm) to avoid any oxidation after filling in a glovebox. For all samples data were collected on an extended angular range (129 degrees in 2theta) with counting times of typically 150s for each of the 457 data points, thus allowing for PDF analysis. Classic corrections (polarization and absorption in cylindrical geometry) were applied before reduction and Fourier transform. Crystallographic data was collected at low temperature (193 K) on a Bruker APEX II Quazar diffractometer equipped with a 30 W air-cooled microfocus source for $[Ru(\eta^4\text{-}C_8H_{12})(\kappa^2\text{-}PPh_2Py)(PPh_2Py)]$ using MoK_α radiation (wavelength = 0.71073 Å). Phi and Omega scans were performed for data collection. Space group was determined on the basis of systematic absences and intensity statistics. An empirical absorption correction was employed. The structures were solved using an intrinsic phasing method (ShelXT).[29] All non-hydrogen atoms were refined anisotropically using the least-square method on *F*.[2,30] Hydrogen atoms were refined isotropically at calculated positions using a riding model. Supplementary crystallographic data can be obtained free of charge from The Cambridge Crystallographic Data Centre via https://www.ccdc.cam.ac.uk/structures. Deposition Number 2382090 (for $[Ru(\eta^4\text{-}C_8H_{12})(\kappa^2\text{-}PPh_2Py)(PPh_2Py)]$) contains the supplementary crystallographic data for this paper. These data are provided free of charge by the joint Cambridge Crystallographic Data Centre and Fachinformationszentrum Karlsruhe Access Structures service. X-ray photoelectron spectroscopy (XPS) experiments under ultra-high vacuum (UHV) were performed with Thermo Scientific K-Alpha apparatus using a monochromatised Al Kα (EAl Kα = 1486.6 eV) X-ray source. The X-ray spot size was about 400 μm. The Pass energy was fixed at 30 eV with a step of 0.1 eV for core levels and 160 eV for surveys (step 1 eV). The spectrometer energy calibration was done using the Au 4f7/2 (83.9 ± 0.1 eV) and Cu 2p3/2 (932.8 ± 0.1 eV) photoelectron lines. XPS spectra were recorded in direct mode N (Ec) and the background signal was removed using the Shirley method. The flood Gun was used to neutralize charge effects on the top surface. Quantitative analyses of the catalytic reaction mixtures were performed via gas chromatography (GC) analyses using internal standard technique and solutions of commercially available products. GC analyses were performed on a SHIMADZU GC-2010 equipped with a SUPELCOWAX 10 capillary column (30 m×0.25 mm×0.25 μm). The method used for quinoline reaction mixture analyses consists on: carrier gas flow, He, 1.25 ml/min; injector temperature, 250 °C; detector (FID) temperature, 250 °C; oven program, 50 °C, hold for 3 min, to 240 °C at 20 °C/min, hold for 10 min for a total run time of 22.5 min; retention time: dodecane, 6.8 min; DHQ, 8.5 and 8.8 min, 5-THQ, 11.8 min; quinoline, 12.3 min; and 1-THQ, 13.0 min.

Synthesis of Metal NPs. In a typical experiment, $[Ru(\eta^4\text{-}C_8H_{12})(\eta^6\text{-}C_8H_{10})]$ and/or $[Ni(\eta^4\text{-}C_8H_{12})_2]$ complexes were introduced in a Fisher Porter bottle, together with PVP or PPh_2Py, and dissolved with THF in a glovebox. The yellow/orange solution was pressurised with 0.3 MPa of H_2 and heated to 85 °C. After some minutes, the solution turned black. The reaction was kept at this temperature overnight under vigorous stirring. Then, the H_2 excess was removed and the colloidal suspension was concentrated under reduced pressure. Pentane was added to precipitate the NPs. After filtration under argon with a cannula, the black solid powder was washed twice with pentane and filtered again before drying under reduced pressure overnight. Additionally, bimetallic RuNi NPs were also prepared using $[Ru(\eta^4\text{-}C_8H_{12})(\kappa^2\text{-}PPh_2Py)(PPh_2Py)]$ and $[Ni(\eta^4\text{-}C_8H_{12})(PPh_2Py)_2]$, the synthesis of which is described below, in combination of $[Ni(\eta^4\text{-}C_8H_{12})_2]$ and $[Ru(\eta^4\text{-}C_8H_{12})(\eta^6\text{-}C_8H_{10})]$, respectively, following the same procedure described above. For each NP studied, the quantities of reactants are detailed hereafter:

Ru/PPh_2Py: 149.8 mg (0.48 mmol) of $[Ru(\eta^4\text{-}C_8H_{12})(\eta^6\text{-}C_8H_{10})]$, 25.0 mg (0.10 mmol) of PPh_2Py, and 40 mL of THF. Yield: 42.0 mg. ICP anal.: 81.8% Ru; 7.3% P.

RuNi/PPh_2Py: 74.9 mg (0.24 mmol) of $[Ru(\eta^4\text{-}C_8H_{12})(\eta^6\text{-}C_8H_{10})]$, 65.3 mg (0.24 mmol) of $[Ni(\eta^4\text{-}C_8H_{12})_2]$, 25.0 mg (0.10 mmol) of PPh_2Py, and 40 mL of THF. Yield: 30.9 mg. ICP anal.: 51.2% Ru; 32.7% Ni; 7.4% P.

Ni/PPh_2Py. 130.6 mg (0.48 mmol) of $[Ni(\eta^4\text{-}C_8H_{12})_2]$, 25.0 mg (0.10 mmol) of PPh_2Py, and 40 mL of THF. Yield: 18.1 mg. ICP anal.: 65.8% Ni; 7.9% P.

RuPNi/PPh_2Py. 100.0 mg (0.14 mmol) of $[Ru(\eta^4\text{-}C_8H_{12})(\kappa^2\text{-}PPh_2Py)(PPh_2Py)]$, 37.4 mg (0.14 mmol) of $[Ni(\eta^4\text{-}C_8H_{12})_2]$ and 40 mL of THF. Yield: 33.7 mg. ICP anal.: 19.8% Ru; 13.4% Ni; 14.8% P.

RuNiP/PPh_2Py. 45.5 mg (0.14 mmol) of $[Ru(\eta^4\text{-}C_8H_{12})(\eta^6\text{-}C_8H_{10})]$, 100.3 mg (0.14 mmol) of $[Ni(\eta^4\text{-}C_8H_{12})(PPh_2Py)_2]$ and 40 mL of THF. Yield: 34.3 mg. ICP anal.: 19.3% Ru; 13.0% Ni; 10.8% P.

Ru/PVP: 140.4 mg (0.45 mmol) of $[Ru(\eta^4\text{-}C_8H_{12})(\eta^6\text{-}C_8H_{10})]$, 150 mg of PVP, and 40 mL of THF. Yield: 102.7 mg. ICP anal.: 24.2% Ru.

RuNi/PVP: 45.0 mg (0.14 mmol) of $[Ru(\eta^4\text{-}C_8H_{12})(\eta^6\text{-}C_8H_{10})]$, 39.2 mg (0.14 mmol) of $[Ni(\eta^4\text{-}C_8H_{12})_2]$, 100 mg of PVP, and 40 mL of THF. Yield: 72.3 mg. ICP anal.: 10.2% Ru; 5.7% Ni.

Ni/PVP: 117.6 mg (0.43 mmol) of $[Ni(\eta^4\text{-}C_8H_{12})_2]$, 150 mg of PVP, and 40 mL of THF. Yield: 114.1 mg. ICP anal.: 15.5% Ni.

Synthesis of $[Ru(\eta^4\text{-}C_8H_{12})(\kappa^2\text{-}PPh_2Py)(PPh_2Py)]$. $[Ru(\eta^4\text{-}C_8H_{12})(\eta^6\text{-}C_8H_{10})]$ (100.1 mg, 0.32 mmol) was dissolved in acetone (10 mL) in a flask in a glovebox. An excess of PPh_2Py (208.1 mg, 0.79 mmol) was added to the yellow solution, which then turned orange and gradually darkened to brown. After six hours of reaction at RT, the solvent was evaporated to dryness. The obtained dark brown solid was washed three times with pentane and dried under vacuum overnight. Crystals suitable for single-crystal X-ray were grown from the slow evaporation of a concentrated solution of $[Ru(\eta^4\text{-}C_8H_{12})(\kappa^2\text{-}PPh_2Py)(PPh_2Py)]$ in acetone-d_6. Yield: 193.3 mg (83%). ^{1}H NMR (400 MHz, THF-d_8): δ (ppm) = 8.35 (br s, H-aromatic, 1H), 7.57 (br m, H-aromatic, 4H), 7.47 (br m, H-aromatic, 2H), 7.33 (br m, H-aromatic, 2H), 7.29 (br m, H-aromatic, 4H), 7.16 (br m, H-aromatic, 6H), 7.06 (br m, H-aromatic, 3H), 6.96 (br m, H-aromatic, 3H), 6.84 (br d, J = 6.8 Hz,H-aromatic, 1H), 6.68 (br s, H-aromatic, 1H), 6.55 (br s, H-aromatic, 1H), 3.41 (br s, H-C_8H_{12}, 1H), 2.54 (br s, H-C_8H_{12}, 1H), 2.17 (br s, H-C_8H_{12}, 1H), 1.86 (br m, H-C_8H_{12}, 5H), 1.55 (br s, H-C_8H_{12}, 1H), 1.26 (br s, H-C_8H_{12}, 1H), 1.10 (br s, H-C_8H_{12}, 1H), 0.92 (br s, H-C_8H_{12}, 1H). $^{31}P\{^1H\}$ NMR (161.9 MHz, THF-d_8): δ (ppm) = 46.8 (s, 1 P), −22.5 (s, 1 P). IR (ATR): ν 3042, 2926, 2796, 1568, 1431, 1087, 802, 737, 691, 504 cm^{-1} Anal. Calcd. for $C_{42}H_{40}N_2P_2Ru$ (735.81 g mol^{-1}): C, 68.56; H, 5.48; N, 3.81; Ru, 13,74; P, 8.42. Found: C, 61.14; H, 4.95; N, 3.33; Ru, 11.7; P, 9.3.

Synthesis of $[Ni(\eta^4\text{-}C_8H_{12})(PPh_2Py)_2]$. The synthesis was carried out following a slightly modified literature procedure.[31] $[Ni(\eta^4\text{-}C_8H_{12})_2]$ (100.0 mg, 0.36 mmol) was dissolved in Et_2O (5 mL) in a flask in a glovebox. PPh_2Py (197.1 mg, 0.75 mmol) was added to the yellow solution and a bright orange precipitate formed immediately. After stirring for 2 h at RT, the solvent was cannulated, and the bright orange solid was washed twice with Et_2O. The resulting solid was dried overnight under reduced pressure. Yield: 216.7 mg (87%). ^{1}H NMR (400 MHz, THF-d_8): δ (ppm) = 8.71 (dd, J = 4.8, 1.9 Hz, H-aromatic, 2H), 7.61 (m, H-aromatic, 8H), 7.21 (m, H-aromatic, 10H), 7.17 (br m, H-aromatic, 2H), 7.12 (m, H-aromatic, 2H), 6.97 (m, H-aromatic, 2H), 6.28 (ddt, J = 7.9, 2.2, 1.1 Hz, H-aromatic, 2H), 4.52 (d, J = 11.2 Hz, H-C_8H_{12}, 4H), 1.47 (t, J = 8.2 Hz, H-C_8H_{12}, 4H), 1.15 (dt, J = 7.1, 2.8 Hz, H-C_8H_{12}, 4H). $^{31}P\{^1H\}$ NMR (161.9 MHz, THF-d_8): δ (ppm) = 36.7 (s, 2 P). IR (ATR): ν 3043, 2951, 2816, 1568, 1430, 1416, 1088, 739, 693, 521, 508, 416 cm^{-1} Anal. Calcd. for $C_{42}H_{40}N_2P_2Ni$ (693.4 g mol^{-1}): C, 72.75; H, 5.81; N, 4.04; Ni, 8.46; P, 8.93. Found: C, 61.72; H, 4.64; N, 4.11; Ni, 10.8; P, 10.5.

Catalytic Hydrogenations. The hydrogenation of quinoline was carried out in a 200 mL stainless steel high-pressure batch Top Industrie reactor. In a typical experiment, a mixture of the catalyst (0.02 mmol of metal), quinoline (516.6 mg, 4 mmol), and dodecane (85.2 mg, 0.5 mmol) as internal standard, in 15 mL of 1-PrOH were loaded into the autoclave inside the glovebox. The autoclave was purged three times with H_2 to remove the inert atmosphere, heated to the desired temperature, and charged with 3.5 MPa of H_2. The stirring rate was fixed at 1200 rpm. Samples of the reaction mixture were taken at different time intervals and analysed by GC. Quantitative analyses of the reaction mixtures were performed via GC using calibration solutions of commercially available products. Filtration tests were performed following the same procedure described above using RuNi/PVP or RuNi/PPh_2Py as catalyst. In this case, the reaction was stopped after three hours of reaction. The catalyst was removed by filtration of the solution through an alumina path. The solution was reintroduced into the reactor, free of solid catalyst. Afterwards, the reactor was pressurised again with 3.5 MPa of H_2, heated at 125 °C, and allowed to react for additional hours at a stirring rate of 1200 rpm. The resulting solution was analysed by GC.

Results and Discussion

Bimetallic RuNi NPs were synthesised by reaction of $[Ru(\eta^4\text{-}C_8H_{12})(\eta^6\text{-}C_8H_{10})]$ and $[Ni(\eta^4\text{-}C_8H_{12})_2]$ with H_2 at 85 °C in the presence of a bidentate ligand, PPh_2Py, following the synthetic methodology described for RuNi/PVP published by some of us elsewhere (Scheme 1).[22] Monometallic Ru and Ni NPs were also synthesised following the same procedure. TEM images of the NPs stabilized with the phosphine ligand show small, spherical and well-dispersed NPs together with agglomerated NPs when the ditopic ligand was used, with mean diameters around 2 nm (Table 1, Figure 1, and Figures S1–S3). Compared to the series of NPs synthesised using PVP,[22] the PPh_2Py-stabilized NPs display slightly larger mean diameters, except in the case of monometallic Ni/PPh_2Py (2.0 ± 0.4 nm), in which the use of this coordinating ligand allowed to decrease substantially the mean size of the NPs compared to Ni/PVP (5.6 ± 1.2 nm). Agglomeration of the NPs was also observed in those bearing the PPh_2Py ligand, the origin of which could be explained by the ditopic nature of the ligand.[18,32,33] Due to the small size of the NPs, EDX analysis was discarded as it is generally a bulk characterization technique and could not provide useful information about the compositional changes in these small NPs.[22] The Ru and Ni content of the samples analysed by ICP-OES is in agreement with the target composition. The estimated P to surface metal atom ratio suggests that about half of the surface metal atoms

$$[Ru(\eta^4\text{-}C_8H_{12})(\eta^6\text{-}C_8H_{10})] + [Ni(\eta^4\text{-}C_8H_{12})_2] + 0.2\ PPh_2Py \xrightarrow[THF,\ 85^oC]{3\ bar\ H_2} RuNi/PPh_2Py + C_8H_{16}$$

Scheme 1. Synthesis of RuNi/PPh_2Py nanoparticles.

Table 1. Metal content and mean size of the metal NPs.

NP	Ru content (%)[a]	Ni content (%)[a]	P content (%)[a]	NP composition (from ICP-OES)	P/$M_{surface}$ ratio[b]	Mean size (nm)[c]
RuNi/PPh_2Py	51.2	32.7	7.4	$Ru_{1.0}$ $Ni_{1.1}$/$PPh_2Py_{0.2}$	0.5	2.1 ± 0.6
Ru/PPh_2Py	81.8	–	7.3	Ru/$PPh_2Py_{0.3}$	0.4	1.4 ± 0.2
Ni/PPh_2Py	–	65.8	7.9	Ni/$PPh_2Py_{0.2}$	0.5	2.0 ± 0.4
RuPNi/PPh_2Py	19.8	13.4	14.8	$Ru_{1.0}Ni_{1.2}$/$PPh_2Py_{1.1}$	1.6	1.3 ± 0.3
RuNiP/PPh_2Py	19.3	13.0	10.8	$Ru_{1.0}Ni_{1.2}$/$PPh_2Py_{0.8}$	1.1	1.1 ± 0.2
RuNi/PVP[d]	10.2	5.7	–	$Ru_{1.0}Ni_{1.0}$/PVP	–	1.5 ± 0.3
Ru/PVP[d]	24.2	–	–	Ru/PVP	–	1.0 ± 0.2
Ni/PVP[d]	–	15.5	–	Ni/PVP	–	5.6 ± 1.2[e]

[a] ICP-OES analysis; in wt%. [b] The percentage of metal in the surface of a given NP was estimated using the mean size of the NP as described in.[22] [c] Mean values of NPs size determined from TEM images by considering at least 200 particles. [d] Data from.[22] [e] Tripodal shaped NPs.

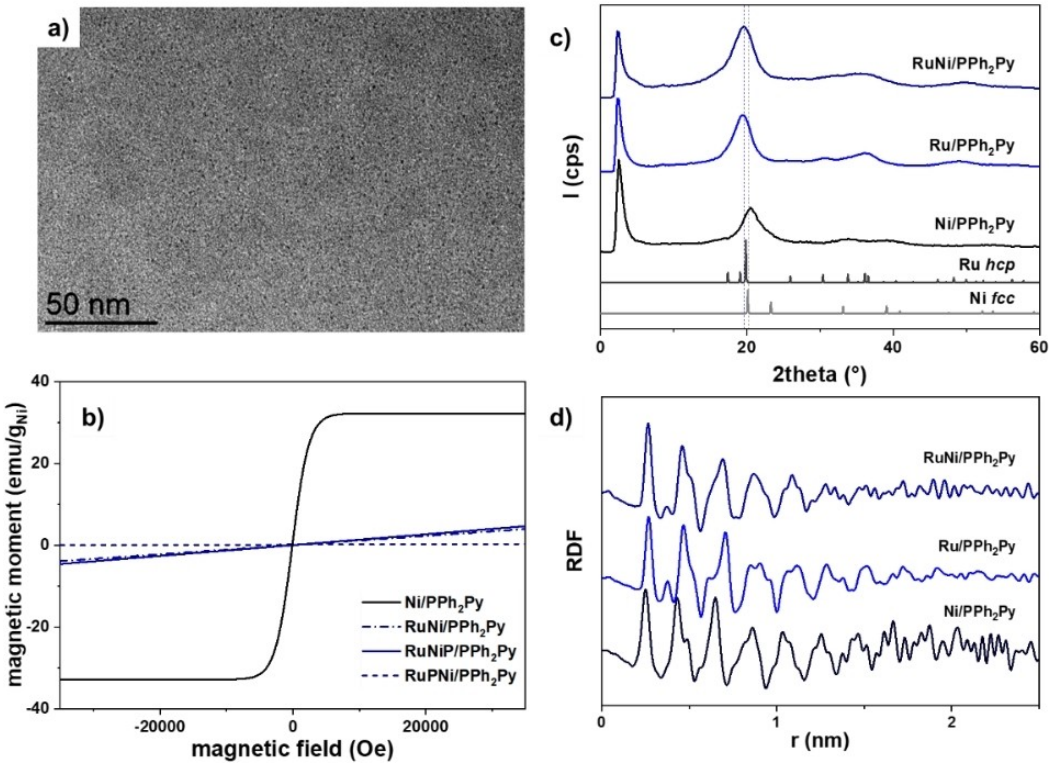

Figure 1. a) TEM image of RuNi/PPh_2Py (scale bar 50 nm); b) magnetic hysteresis cycles of bimetallic and monometallic nanoparticles measured at room temperature; c) diffractograms of RuNi/PPh_2Py, Ru/PPh_2Py, and Ni/PPh_2Py together with the reference of Ru hcp and Ni fcc structures; and d) related radial distribution functions (RDFs).

could be coordinated to a phosphine ligand, see Table 1 for details. Magnetic properties of the NPs stabilized with PPh_2Py, analysed by SQUID magnetometry, point to a bimetallic nature of the RuNi/PPh_2Py NPs, as a decrease on the magnetisation is observed for RuNi/PPh_2Py NPs when compared to the monometallic Ni NPs. This phenomenon is expected upon incorporation of Ru onto the Ni structure.[34,35] Figure 1b, and S6 provide the hysteresis cycles recorded for the bimetallic RuNi and monometallic Ni NPs measured at RT and corrected of the diamagnetic contribution of PPh_2Py and PVP. More details about the magnetic properties are given in SI.

In order to confirm the coordination of the stabilizing ligand onto the surface and identify its coordination mode, a series of experiments were set up and characterization techniques such as XPS, IR and NMR were utilized. First, Ru(0) and Ni(0) complexes bearing PPh_2Py were synthesised. [Ru(η^4-C_8H_{12})(η^6-C_8H_{10})] and [Ni(η^4-C_8H_{12})$_2$] reacted smoothly with the phosphine ligand, particularly the Ni(0) complex which produced the desired product instantly. [Ni(η^4-C_8H_{12})(PPh_2Py)$_2$] was synthesised following a slightly modified described procedure.[31] The bright orange solid was isolated in an 87% yield. The $^{31}P\{^1H\}$ NMR spectrum of [Ni(η^4-C_8H_{12})(PPh_2Py)$_2$] in THF-d_8 displays the

expected singlet peak of the coordinated phosphines in a monodentate mode at 36.7 ppm. Upon reaction of the Ru complex, [Ru(η^4-C_8H_{12})(η^6-C_8H_{10})] with two equivalents of PPh_2Py, a brown solid was isolated in an 83% yield. $^{31}P\{^1H\}$ NMR spectrum of the solution of the brown solid in THF-d_8 displays two distinctive singlets at considerable different chemical shifts, 46.8 and −22.5 ppm, both integrating for one phosphorus. The singlet at about 40 ppm is consistent with a coordination of the phosphorus atom of the ligand to the Ru atom in a monodentate manner. The signal at low frequency reveals a second ligand coordinated to the Ru atom in a bidentate manner.[36–38] ^1H NMR spectrum confirms the presence of two ligands and a cyclooctadiene moiety in the metallic complex. Single crystals of [Ru(η^4-C_8H_{12})(κ^2-PPh_2Py)(PPh_2Py)] suitable for X-ray diffraction were obtained by slow evaporation of a solution of the complex in acetone (Figure 2). The structure corroborates the findings ascertained by NMR. The Ru and Ni complexes bearing the P, N ligand were further used to synthesise RuNi bimetallic NPs, RuPNi/PPh_2Py and RuNiP/PPh_2Py, with the corresponding counterparts, [Ni(η^4-C_8H_{12})$_2$] and [Ru(η^4-C_8H_{12})(η^6-C_8H_{10})], respectively, following the same procedure described for RuNi/PPh_2Py (Scheme 1). TEM analyses of RuPNi/PPh_2Py and RuNiP/PPh_2Py display small, spherical and well dispersed NPs (Figure S4 and S5); mean sizes are smaller than those observed for RuNi/PPh_2Py, which could be attributed to the larger amount of ligand present during the reaction (Table 1).[39] ^1H, ^{13}C and ^{31}P MAS NMR on the solid-state were recorded for this series of nanomaterials, in order to assess if the phosphine is coordinated onto the metallic surface and to identify its coordination mode. The ^1H MAS NMR signals are consistent with H atoms of aromatic rings, characterised by a broad resonance centred at about 6.5 ppm (Figure S7). The same observation is revealed by the ^{13}C CP-MAS NMR spectra of the compounds, as signals centred at about 127 ppm are obtained for all materials, chemical shifts consistent with the aryl moieties of the P, N ligand (Figure S8). The $^{31}P\{^1H\}$ MAS NMR spectra of [Ru(η^4-C_8H_{12})(κ^2-PPh_2Py)(PPh_2Py)] and [Ni(η^4-C_8H_{12})(PPh_2Py)$_2$] (Figure 3 and S9) show two sharp signals at 50.1 and −27.0 ppm, and at ca. 36.7 ppm, respectively, in line with the $^{31}P\{^1H\}$ NMR recorded in solution. The $^{31}P\{^1H\}$ Hahn-

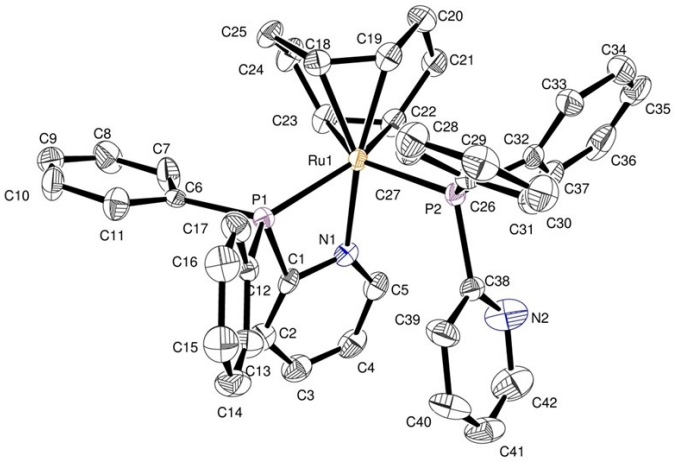

Figure 2. Molecular structure of the neutral ruthenium complex [Ru(η^4-C_8H_{12})(κ^2-PPh_2Py)(PPh_2Py)] showing the bidentate coordination of PPh_2Py. Selected bond distances (Å) and angles (deg): N1–Ru1: 2.129(4); P1–Ru1: 2.3414(14); P2–Ru1: 2.3155(13); N1–Ru1–P2: 91.75(12); P2–Ru1–P1: 107.37(5); N1–Ru1–P1: 67.89(12). Hydrogen atoms are omitted for clarity. Thermal ellipsoids are drawn at 50% probability. Color code for atoms: Ru: orange; P: pink; N: blue; C: grey.

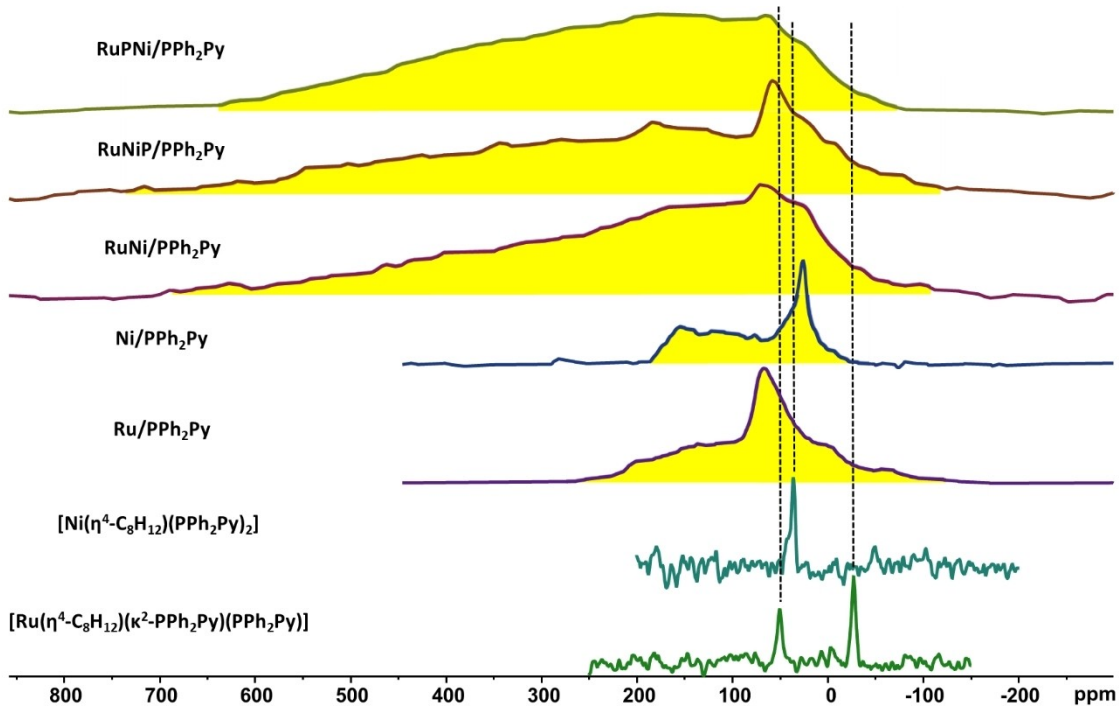

Figure 3. $^{31}P\{^1H\}$ Hahn-echo MAS NMR (relaxation delay of 10 s) of the monometallic Ru/PPh_2Py and Ni/PPh_2Py NPs, bimetallic RuNi/PPh_2Py, RuPNi/PPh_2Py, and RuNiP/PPh_2Py NPs, together with [Ru(η^4-C_8H_{12})(κ^2-PPh_2Py)(PPh_2Py)] and [Ni(η^4-C_8H_{12})(PPh_2Py)$_2$] complexes.

echo MAS NMR spectra of the NPs show depending on the case, more or less sharp or very broad signals. For all the NPs, the proportion of the very broad components of the ^{31}P spectra is relatively important. In fact, the very broad signals are only partially measured with a standard $^{31}P\{^{1}H\}$ Hahn-echo MAS NMR experiment used to record the spectra of Figure 3. To fully detect the broad ^{31}P signals, it is necessary to use the variable offset cumulative spectra (VOCS) technique[28] and a very short recovery delay of 0.1 s, associated with the very short ^{31}P T_1 relaxation times for these species (an example is provided in Figure S10). This fast relaxation coupled to the high frequency shifts is characteristic of the presence of the Knight shift effect. This is a paramagnetic effect that reflects the local magnetic field produced by the magnetization of the conduction electrons in metals, that was observed on metallic NPs of size larger than 2 nm.[40] Despite the small size of the NPs ascertained by TEM, the Knight shift effect is clearly present in all the samples (Figure S10). Thus, it is probably associated to the aggregates of NPs that were observed in the samples. However, the Knight shift effect confirms the coordination of the P atoms on the surface of the NPs, as this effect is only observed for atoms directly bonded to the metallic surfaces, thus also explaining why no evidence of such broad components were seen in ^{1}H and ^{13}C MAS NMR. Unfortunately, the Knight shift makes the analysis of the ^{31}P spectra more complicated, notably to determine if the coordination mode is mono- or bi-dentate. In Figure 3 and S9, some sharp signals, however broader than those of the molecular complexes, can be detected in the 20 to 70 ppm range and are probably associated to the smallest isolated NPs (which do not exhibit the Knight shift effect). These sharp signals are in agreement with phosphine ligand coordinated in a monodentate fashion onto the metallic surface. Ru/PPh_2Py and Ni/PPh_2Py showed a main signal at 67 and 27 ppm, respectively. Note that for Ru/PPh_2Py, a broad shoulder centred at ca. −2 ppm is also observed, that could eventually correspond to a bidentate coordination mode. In the three bimetallic systems, RuPNi/PPh_2Py, RuNiP/PPh_2Py and RuNi/PPh_2Py, two main sharp signals are also observed respectively at 63 and 23, 58 and 21, and 69 and 24 ppm, indicating that the phosphine is both coordinated to Ru and Ni atoms in a monodentate manner. As for Ru/PPh_2Py, a significant amount of broad signal at low frequency in the −20–20 ppm range is also detected that may correspond to the bidentate mode. These observations are in agreement with a bimetallic system in which both metals are present at the surface, or a mixture of monometallic NPs; nevertheless, the latter scenario is discarded as WAXS analyses show that the RuNi/PPh_2Py displays features consistent with a bimetallic core-shell structure in which Ni is preferentially on the surface, see Figure 1 and SI for discussion. Also, magnetic measurements are in agreement with the bimetallic nature of these species, see above and SI. In addition, the phosphine did not present any preference of coordination towards a specific metal, even when preformed Ru and Ni complexes bearing the P, N ligand were used as starting material. For RuNiP/PPh_2Py and RuPNi/PPh_2Py, in which a ligand to surface ratio was estimated to be one, no free phosphine was evidenced in the MAS NMR spectra, thus, probably a high phosphine coverage can be obtained using this procedure.

ATR-FTIR analyses were performed in a glovebox for all the synthesised NPs. The spectra are depicted in Figure 4 and S12 including PPh_2Py and [Ru(η^4-C_8H_{12})(κ^2-PPh_2Py)(PPh_2Py)] and [Ni(η^4-C_8H_{12})(PPh_2Py)$_2$] complexes. The spectra confirm the presence of the ligand in all the nanomaterials, in line with NMR analyses. Ru/PPh_2Py and Ni/PPh_2Py NPs display similar spectra, showing characteristic absorption bands of the PPh_2Py ligand, such as C=C and/or C=N stretching ca. 1500 cm^{-1}, C–N stretching ca. 1000 cm^{-1} and the =C–H bending ca. 700 cm^{-1}. In the bimetallic systems, besides the absorption bands of the ligand, some intense new bands at 1250 and 800 cm^{-1} are observed, which are attributed to P=O and P–C=N vibrations, respectively. The later band, at 800 cm^{-1}, is consistent with a

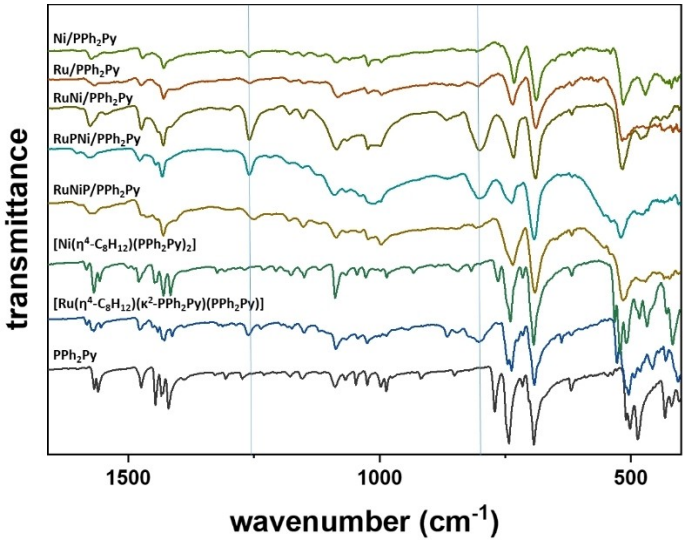

Figure 4. ATR-IR spectra of the monometallic Ru/PPh_2Py and Ni/PPh_2Py NPs, the bimetallic RuNi/PPh_2Py NPs, RuPNi/PPh_2Py, and RuNiP/PPh_2Py, the [Ru(η^4-C_8H_{12})(κ^2-PPh_2Py)(PPh_2Py)] and [Ni(η^4-C_8H_{12})(PPh_2Py)$_2$] complexes, and the PPh_2Py ligand.

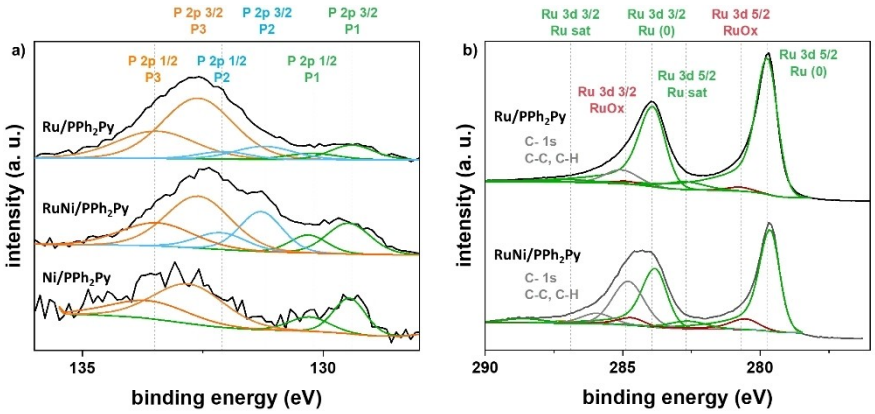

Figure 5. XPS high-resolution scan spectra of a) P 2p and b) C 1s and Ru 3d.

chelate coordination of the P, N ligand. RuPNi/PPh_2Py and RuNi/PPh_2Py display this vibration band as in the [Ru(η^4-C_8H_{12})(κ^2-PPh_2Py)(PPh_2Py)] complex. This observation indicates a mixture of coordination modes for the P, N ligand onto RuNi bimetallic NPs. These could suggest that some amounts of the ligand are chelated, in agreement with some ^{31}P MAS NMR signals observed at low frequency (between −20 and 20 ppm).

XPS analyses were performed on monometallic Ru/PPh_2Py and Ni/PPh_2Py and bimetallic RuNi/PPh_2Py NPs, Figure 5 depicts some selected spectra. Survey spectra and high-resolution scan spectra together with the fitting peaks of the corresponding components are presented in Figures S13–S15; Table S2 summarizes binding energies (BE) together with the concentration of the fitted peaks in atomic % of the three samples. Ru/PPh_2Py displays a Ru $3d_{5/2}$ peak at 279.7 eV, slightly lower than that expected for metallic Ru, 280.0 eV,[41] indicating that Ru has a richer electronic environment, that could be due to the presence of the phosphine coordinated onto the metallic surface. Further, bimetallic RuNi/PPh_2Py shows a Ru $3d_{5/2}$ peak at 279.6 eV, thus lower BE than monometallic Ru NPs. This lower BE has been attributed to the close vicinity of Ni to Ru on the bimetallic NPs and due to the different electronegativity of metals, Ni providing electronic density to Ru, as observed in some other RuNi systems.[42,43] A shift in BE can be observed as well in the Ni $2p_{3/2}$ peak of RuNi/PPh_2Py with respect to Ni/PPh_2Py. Ni/PPh_2Py shows a BE of 852.7 eV, while RuNi/PPh_2Py displays a lower BE, 852.5 eV. The observed shift in BE cannot be attributed to the presence of a more electronegative metal, yet, the RuNi/PPh_2Py sample shows that Ni is more oxidized than in Ni/PPh_2Py sample; probably due to the fact that the manipulation of samples for XPS was not completely performed in an inert atmosphere, the origin of the oxidation of Ni in the sample cannot be unequivocally determined, but the presence of NiOx and Ni–OH probably plays a role in the shift of the BE observed for Ni $2p_{3/2}$ in the RuNi/PPh_2Py sample. On the other hand, the BE of Ni $2p_{3/2}$ peak of metallic Ni was not clearly affected by the presence of the phosphine ligand, as in both Ni/PPh_2Py and RuNi/PPh_2Py, the BE attributed to this component was very close to that expected value of metallic Ni, 852.8 eV. Three doublet peaks are observed in the P 2p region for Ru/PPh_2Py and RuNi/PPh_2Py, and two for Ni/PPh_2Py, indicating the coexistence of phosphorus atoms with different electronic states (Figure 5). The main species appearing in the three samples at similar BE: 132.6, 132.6 and 132.8 eV for P $2p_{3/2}$ for Ru/PPh_2Py, RuNi/PPh_2Py, and Ni/PPh_2Py, respectively; and 133.5, 133.5 and 133.6 eV for P $P2p_{1/2}$ for Ru/PPh_2Py, RuNi/PPh_2Py, and Ni/PPh_2Py, respectively, which is consistent with the phosphine coordinated to metal.[44,45] The similarity of BE between Ru/PPh_2Py and Ni/PPh_2Py for this doublet peak did not allow confirmation of the expected higher Ni amount on the surface for the bimetallic sample. At lower BE, one set of doublets appears for all samples around 129.5 and 130.3 eV, which could be attributed to the presence of free phosphine or the presence of Ru and/or Ni phosphides.[46] As solid-state NMR has not shown the presence of free ligand either the presence of phosphine oxide, a possibility is that that some phosphide was produced during the synthetic procedure, as previously observed for other Ni NPs.[44] It is noteworthy to point that this phosphide species are more abundant in Ni/PPh_2Py, thus some species attributed as NiOx of Ni–OH in the Ni $2p_{3/2}$ could have a contribution of NiPx species, as they similarly appear at higher BE than metallic Ni $2p_{3/2}$ (852.8 eV). A third P contribution was observed for Ru containing samples, Ru/PPh_2Py and RuNi/PPh_2Py, as a double at 131.2 and 132.1 eV. This species was tentatively attributed to a chelate coordination of the P, N ligand, which is in line with IR and NMR analyses. For comparative purposes, XPS analyses of [Ru(η^4-C_8H_{12})(κ^2-PPh_2Py)(PPh_2Py)] and [Ni(η^4-C_8H_{12})(PPh_2Py)$_2$] complexes were performed (Figure S16 and S17, Table S3). The high degree of oxidation of the samples, resulting from the inability to conduct manipulations entirely in an inert atmosphere, prevents definitive conclusions from being drawn.

Thus, core-shell RuNi NPs in which Ru is on the core were synthesised in the presence of PPh_2Py, a similar structure as previously observed for RuNi NPs stabilized in PVP.[22] The presence of a chelating phosphine did not produce the desired alloy structure, yet WAXS analyses showed that the structure is more complex with respect to RuNi/PVP, pointing to a partial alloyed structure. Solid-state NMR, IR and XPS confirm the presence of the phosphine ligand onto the surface, mainly

coordinated in a monodentate manner indistinctly on Ru or Ni, thus pointing to the presence of both metals on the surface.

The catalytic properties of RuNi/PPh_2Py together with the monometallic and PVP counterparts were evaluated in the hydrogenation of quinoline. Optimization of the catalytic reaction conditions is presented in the SI using RuNi/PVP (Table S4, Figures S18 and S19). Taking into consideration these results, the series of catalysts was tested at 125 °C under 3.5 MPa of H_2 in 1-PrOH (Table 2, Figure 6). Ru monometallic catalysts were highly active, as expected for a Ru based catalysts, which usually hydrogenate heteroaromatic rings under mild reaction conditions.[3,20] It is observed that the presence of the phosphine ligand increases the activity of the Ru NPs (TOF of 379 h^{-1} for Ru/PPh_2Py and 231 h^{-1} for Ru/PVP) and slightly increases the selectivity of the process, as only the hydrogenation of the N-bearing cycle is observed, as we previously hypothesised. Ni based catalysts were comparably much less active to Ru based ones, and no synergetic effect was observed between the metals. For monometallic Ni NPs, the introduction of the PPh_2Py ligand also increased the activity but in a limited manner. Concerning the bimetallic NPs, RuNi/PVP were slightly more active than RuNi/PPh_2Py (TOF of 30 h^{-1} for RuNi/PPh_2Py and 45 h^{-1} for RuNi/PVP), thus the opposite

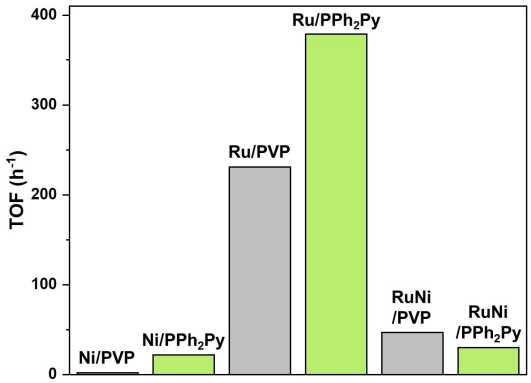

Figure 6. Turnover frequency of Ru, Ni and RuNi nanoparticles.

observation. Taking into consideration that a priori the presence of the phosphine has a beneficial effect on activity, the difference on activity could be attributed to a different structure of the bimetallic NPs. Examining the estimation of the Ni coverage on the RuNi NPs reveals that RuNi/PVP displays a 77% of Ni coverage,[22] whereas RuNi/PPh_2Py is estimated to be close to 100% (Table S1). Consequently, Ru atoms are theoretically

Table 2. Selective hydrogenation of quinoline in 1-PrOH at 125 °C under 3.5 MPa of H_2.[a]

Entry	Catalyst	TOF (h^{-1})[b,c]	Time (h)	Conversion (%)[c]	1-THQ (%)[c]	5-THQ (%)[c]	DHQ (%)[c]	Metal leaching (mmol, %)
1	RuNi/PPh_2Py	30	1	7	>99	<1	–	
2			3	15	>99	<1	–	
3			5	62	>99	<1	–	
4			24	84	>99	<1	–	8.5×10^{-4}, 4%
5	Ru/PPh_2Py	379	1	93	>99	<1	–	
6			3	>99	>99	<1	–	
7			5	>99	>99	<1	–	
8			24	>99	>99	<1	–	1.6×10^{-5}, 0.1%
9	Ni/PPh_2Py	22	1	5	>99	<1	–	
10			3	13	>99	<1	–	
11			5	17	>99	<1	–	
12			24	36	>99	<1	–	7.2×10^{-5}, 0.4%
13	RuNi/PVP	47	1	10	>99	<1	–	
14			3	30	>99	<1	–	
15			5	56	>99	<1	–	
16			24	97	>99	<1	traces	8.5×10^{-4}, 4%
17	Ru/PVP	231	1	83	96	4	–	
18			3	98	96	3	1	
19			5	>99	96	3	1	
20			24	>99	93	3	4	1.5×10^{-4}, 0.8%
21	Ni/PVP	–	1	<1	>99	–	–	
22		22*	3	4	>99	traces	–	
23			5	9	>99	traces	–	
24			24	26	>99	traces	–	1.6×10^{-4}, 0.8%

[a] Reaction conditions: 2×10^{-2} mmol of metal, 4 mmol of QN, 0.5 mmol of dodecane (internal standard), 3.5 MPa of H_2, 125 °C, 15 mL of 1-PrOH. [b] TOFs calculated at 1 h (* at 3 h) of reaction according to the surface amount of metal. [c] Determined by GC using an internal standard technique.

more accessible on the surface of RuNi/PVP. This higher availability of Ru content on RuNi/PVP, could explain its higher activity compared to RuNi/PPh_2Py, and indirectly confirm[47] the structure of the bimetallic NPs ascertained by the characterization techniques described above. Regarding the robustness of the catalysts, it was observed on Ni based catalysts that the catalytic solution turned slightly yellow after 24 h of reaction, pointing out towards a leaching of metallic homogeneous species (Figure S20). ICP analyses of the catalytic solution after filtration over an alumina path confirmed the leaching of metallic species in all cases, ranging from 0.1 to 4% relative to the engaged metal. TEM after catalysis showed that the NPs were not stable under the reaction conditions displaying in all cases an increase of the NP size (Figure S21–26, Table S5). Filtration tests were performed using RuNi/PPh_2Py and RuNi/PVP as catalysts. The conversion after removal of the catalysts was similar to the unfiltered reaction analogues (Figure S27). These results point to the leaching issues of these NPs under these relatively harsh reaction conditions (125 °C, 3.5 MPa H_2), as also revealed by ICP analyses of the filtered solution. This is in clear contrast with our previous results for the hydrogenation of furfural using RuNi/PVP as catalysts, the materials were stable under similar reaction conditions.[22] Thus, as at the selected temperature, pressure, and solvent, the colloidal NPs are stable, a plausible explanation could be that the presence of basic compounds, mainly quinoline and tetrahydroquinoline, may play a role in the robustness of the tested catalysts, specifically the Ni based ones. The hypothesis needs to be confirmed, but if so the leaching issues could not be avoided. We discarded to work at lower temperatures due to the low activity observed under these conditions (Figure S18). We are currently performing supplementary studies to assess the nature of this active Ni molecular species or clusters. Ni based homogeneous catalysts are scarce for this application, and of high interest.[48,49]

Conclusions

In this work, RuNi NPs were successfully synthesised for the first time using a bidentate P, N ligand. The use of several characterization techniques, in combination with the synthesis and characterisation of Ru and Ni complexes bearing the same ligand allows us to propose that the bidentate ligand is mainly coordinated by the P atom, as similarly observed in previous works dealing with P ligands as metal NPs stabilizers. It is also observed that some bidentate coordination to the surface is possible, which could explain the observed agglomeration of the NPs. The application of these bimetallic NPs as catalysts for the hydrogenation of quinoline revealed that the RuNi based colloidal species were not robust under these reaction conditions, probably due to the presence of basic quinoline derivatives, and that the combination of both metallic atoms did not show a synergistic effect between the metals, in contrast with our previous findings. Yet, the presence of the donor phosphorus ligand had a beneficial effect as it increased the activity and selectivity of the process for the Ru monometallic nanocatalyst, and also allowed the synthesis of small monometallic Ni NPs. This work also introduces new perspectives in the field of the hydrogenation of (hetero)arenes using molecular Ni catalysts. On the other hand, an open question remains about the robustness of Ni-based nanocatalysts in the presence of strong bases under relatively harsh reaction conditions.

Supporting Information Summary

The authors have cited additional references within the Supporting Information.[50–53] The Supporting Information includes TEM images of the nanoparticles, as-synthesised and after catalysis, along with their respective size histograms; details on the estimation of Ni coverage; additional information in the magnetic properties of the nanoparticles; additional solid-state NMR spectra; IR and WAXS analyses; XPS analyses, including Tables with binding energies, full survey spectra, and high-resolution scan spectra of several elements for nanoparticles stabilized with PPh_2Py, and [Ru(η^4-C_8H_{12})(κ^2-PPh_2Py)(PPh_2Py)] and [Ni(η^4-C_8H_{12})(PPh_2Py)$_2$] molecular complexes; catalytic results for the optimization of the experimental conditions; a picture of several catalytic reaction mixtures after catalysis; and the time-concentration curves of the filtration tests.

Author Contributions

M. Cardona-Farreny synthesised and participated in the characterization of the catalysts, also performed catalytic studies, H. Ishikawa performed catalytic studies and participated in the characterization of the catalysts, A. O. Odufejo Ogoe synthesised and participated in the characterization of the catalysts, also performed some catalytic studies, S. Mallet-Ladeira performed XRD studies and interpreted the results. Y. Coppel performed solid-state NMR analyses and interpreted the results. P. Lecante performed the WAXS analyses and interpreted the results. J. Esvan performed the XPS analyses and interpreted the results. K. Philippot participated in the supervision of the work. M. Rosa Axet participated in the conceptualization, funding acquisition, writing - review and editing, supervision.

Acknowledgements

This work was supported by the CNRS and Université de Toulouse-Paul Sabatier, which we gratefully acknowledge. The authors acknowledge the financial support from the Ministère de l'enseignement supérieur et de la recherche for M. C.-F. grant and from the Japan Society for the Promotion of Science (JSPS) for H. I. grant. R. Castaing characterization platform in Toulouse is also acknowledged.

Conflict of Interests

The authors declare no conflict of interest.

Data Availability Statement

The data that support the findings of this study are available from the corresponding author upon reasonable request.

Keywords: Heterogeneous catalysis · Heteroarene · Hydrogenation · Bimetallic · Ruthenium · Nickel

[1] K. M. P. Wheelhouse, R. L. Webster, G. L. Beutner, *Org. Process Res. Dev.* **2023**, *27*(7), 1157–1159.
[2] R. M. Bullock, J. G. Chen, L. Gagliardi, P. J. Chirik, O. K. Farha, C. H. Hendon, C. W. Jones, J. A. Keith, J. Klosin, S. D. Minteer, et al. *Science* **2020**, *369*(6505), eabc3183. DOI: 10.1126/science.abc3183.
[3] M. P. Wiesenfeldt, Z. Nairoukh, T. Dalton, F. Glorius, *Angew. Chem., Int. Ed.* **2019**, *58*(31), 10460–10476.
[4] M. A. Rivero-Crespo, P. Rubio-Marques, J. C. Hernandez-Garrido, M. Mon, J. Oliver-Meseguer, A. Leyva-Perez, *Catal. Sci. Technol.* **2023**, *13*(8), 2508–2516.
[5] Y. Ren, Y. Yang, M. Wei, *ACS Catal.* **2023**, *13*(13), 8902–8924.
[6] Y. Hu, M. Liu, S. Bartling, H. Lund, H. Atia, P. J. Dyson, M. Beller, R. V. Jagadeesh, *Sci. Adv.* **2023**, *9*(48), eadj8225. DOI: 10.1126/sciadv.adj8225.
[7] Z. Yuan, X. Li, G. Wang, Z. Zhu, Y. Liao, Z. Zhang, B. Liu, *Mol. Catal.* **2023**, *540*, 113052.
[8] L. Niu, Y. An, X. Yang, G. Bian, Q. Wu, Z. Xia, G. Bai, *Mol. Catal.* **2021**, *514*, 111855.
[9] M. Puche, L. Liu, P. Concepcion, I. Sorribes, A. Corma, *ACS Catal.* **2021**, *11*(13), 8197–8210. DOI: 10.1021/acscatal.1c01561 .
[10] S. Guo, Y. Wu, C. Wang, Y. Gao, M. Li, B. Zhang, C. Liu, *Nat. Commun.* **2022**, *13*(1), 5297.
[11] H. Yang, M. Xu, L. Zhang, W. Fang, E. Liu, H. Zhang, *Microporous Mesoporous Mater.* **2023**, *360*, 112701.
[12] F. Chen, A.-E. Surkus, L. He, M.-M. Pohl, J. Radnik, C. Topf, K. Junge, M. Beller, *J. Am. Chem. Soc.* **2015**, *137*(36), 11718–11724.
[13] C. Bauer, F. Mueller, S. Keskin, M. Zobel, R. Kempe, *Chem. - Eur. J.* **2023**, *29*(30), e202300561.
[14] Y. Hu, X. Li, M. Liu, S. Bartling, H. Lund, J. Rabeah, P. J. Dyson, M. Beller, R. V. Jagadeesh, *ChemCatChem.* **2024**, *16*(1), e202301027.
[15] W. Li, X. Cui, K. Junge, A.-E. Surkus, C. Kreyenschulte, S. Bartling, M. Beller, *ACS Catal.* **2019**, *9*(5), 4302–4307.
[16] N. Hammi, S. Chen, C. Michon, S. Royer, A. El Kadib, *Mol. Catal.* **2022**, *519*, 112104.
[17] B. Sahoo, C. Kreyenschulte, G. Agostini, H. Lund, S. Bachmann, M. Scalone, K. Junge, M. Beller, *Chem. Sci.* **2018**, *9*(42), 8134–8141.
[18] F. Leng, I. C. Gerber, P. Lecante, S. Moldovan, M. Girleanu, M. R. Axet, P. Serp, *ACS Catal.* **2016**, *6*, 6018–6024.
[19] Z. Luo, Y. Min, D. Nechiyil, W. Bacsa, Y. Tison, H. Martinez, P. Lecante, I. C. Gerber, P. Serp, M. R. Axet, *Catal. Sci. Technol.* **2019**, *9*, 6884–6898.
[20] V. Colliere, M. Verelst, P. Lecante, M. R. Axet, *Chem. - Eur. J.* **2024**, *30*(13), e202302131.
[21] Z. Wei, F. Shao, J. Wang, *Chin. J. Catal.* **2019**, *40*(7), 980–1002.
[22] M. Cardona-Farreny, P. Lecante, J. Esvan, C. Dinoi, I. Del Rosal, R. Poteau, K. Philippot, M. R. Axet, *Green Chem.* **2021**, *23*, 8480–8500.
[23] S. Fujita, K. Nakajima, J. Yamasaki, T. Mizugaki, K. Jitsukawa, T. Mitsudome, *ACS Catal.* **2020**, *10*(7), 4261–4267.
[24] J.-q. Bai, M. Tamura, Y. Nakagawa, K. Tomishige, *Catal. Sci. Technol.* **2022**, *12*(8), 2420–2425. DOI: 10.1039/d2cy00383j.
[25] S. Mao, P. Ryabchuk, S. Dastgir, M. Anwar, K. Junge, M. Beller, *ACS Appl. Nano Mater.* **2022**, *5*(4), 5625–5630.
[26] T. Zhu, L. Liu, Y. Zhao, M. Gao, Y. Dong, D. Xia, P. Huang, H. Cheng, M. Yang, *Chem. Eng. J.* **2024**, *493*, 152354.
[27] K. Wang, Z. Cao, J. Wang, Z.-H. He, D. Wang, R.-R. Zhang, W. Wang, Y. Yang, Z.-T. Liu, *Mol. Catal.* **2022**, *520*, 112166.
[28] L. R. Lichty, J. W. Han, R. Ibanez-Meier, D. R. Torgeson, R. G. Barnes, E. F. W. Seymour, C. A. Sholl, *Phys. Rev. B* **1989**, *39*(4), 2012.
[29] G. M. Sheldrick, *Acta Crystallogr., Sect. A* **2015**, *71*(1), 3–8.
[30] G. M. Sheldrick, *Acta Crystallogr., Sect. C* **2015**, *71*(1), 3–8.
[31] H. Maciejewski, A. Sydor, B. Marciniec, M. Kubicki, P. B. Hitchcock, *Inorg. Chim. Acta* **2006**, *359*(9), 2989–2997.
[32] Y. Min, F. Leng, B. F. Machado, P. Lecante, P. Roblin, H. Martinez, T. Theussl, A. Casu, A. Falqui, M. Barcenilla, et al., *Eur. J. Inorg. Chem.* **2020**, *2020*(43), 4069–4082.
[33] Y. Min, H. Nasrallah, D. Poinsot, P. Lecante, Y. Tison, H. Martinez, P. Roblin, A. Falqui, R. Poteau, I. del Rosal, et al., *Chem. Mater.* **2020**, *32*(6), 2365–2378.
[34] Y. Takahashi, R. L. Jacobs, *J. Phys. F* **1982**, *12*(3), 517–528.
[35] B. Michelutti, R. Perrier de la Bathie, E. Du Tremolet de Lacheisserie, A. Magnetization Waintal, *Solid State Commun.* **1978**, *28*(10), 879–882.
[36] R. Garcia-Alvarez, S. E. Garcia-Garrido, J. Diez, P. Crochet, V. Cadierno, *Eur. J. Inorg. Chem.* **2012**, *2012*(26), 4218–4230.
[37] P. Kumar, A. K. Singh, R. Pandey, D. S. Pandey, *J. Organomet. Chem.* **2011**, *696*(22), 3454–3464.
[38] M. Angoy, M. V. Jimenez, F. J. Modrego, L. A. Oro, V. Passarelli, J. J. Perez-Torrente, *Organometallics* **2018**, *37*(16), 2778–2794.
[39] L. Lu, S. Zou, B. Fang, *ACS Catal.* **2021**, *11*(10), 6020–6058.
[40] J. M. Asensio, S. Tricard, Y. Coppel, R. Andres, B. Chaudret, E. de Jesus, *Chem. - Eur. J.* **2017**, *23*(54), 13435–13444.
[41] D. E. Starr, H. Bluhm, *Surf. Sci.* **2013**, *608*, 241–248.
[42] M. Li, H. Wang, W. Zhu, W. Li, C. Wang, X. Lu, *Adv. Sci.* **2020**, *7*, 1901833. DOI: 10.1002/advs.201901833.
[43] P.-F. Zhang, J.-Y. Zhang, T. Sheng, Y.-Q. Lu, Z.-W. Yin, Y.-Y. Li, X.-X. Peng, Y. Zhou, J.-T. Li, Y.-J. Wu, et al., *ACS Catal.* **2020**, *10*(2), 1640–1651.
[44] S. Carenco, Z. Liu, M. Salmeron, *ChemCatChem.* **2017**, *9*(12), 2318–2323.
[45] L. M. Martinez-Prieto, S. Carenco, C. H. Wu, E. Bonnefille, S. Axnanda, Z. Liu, P. F. Fazzini, K. Philippot, M. Salmeron, B. Chaudret, *ACS Catal.* **2014**, *4*, 3160–3168.
[46] B. Elsener, D. Atzei, A. Królikowski, A. Rossi, *Surf. Interf. Anal.* **2008**, *40*(5), 919–926.
[47] X. Qi, M. R. Axet, K. Philippot, P. Lecante, P. Serp, *Dalton Trans.* **2014**, *43*(24), 9283–9295.
[48] K. Michaliszyn, E. S. Smirnova, A. Bucci, V. Martin-Diaconescu, J. Lloret Fillol, *ChemCatChem.* **2022**, *14*(11), e202200039.
[49] M. L. G. Sansores-Paredes, M. Lutz, M.-E. Moret, *Nat. Chem.* **2024**, *16*(3), 417–425.
[50] A. Roy, V. Srinivas, S. Ram, T. V. C. Rao, *J. Phys.: Condens. Matter* **2007**, *19*, 346220/346221–346220/346216. DOI: 10.1088/0953-8984/19/34/346220.
[51] L. Zaramello, B. L. Albuquerque, J. B. Domingos, K. Philippot, *Dalton Trans.* **2017**, *46*, 5082–5090.
[52] C. Bergounhou, C. Blandy, R. Choukroun, P. Lecante, C. Lorber, J.-L. Pellegatta, *New J. Chem.* **2007**, *31*, 218–223.
[53] V. Kelsen, A. Meffre, P.-F. Fazzini, P. Lecante, B. Chaudret, *ChemCatChem.* **2014**, *6*, 1714–1720.

Manuscript received: July 31, 2024
Revised manuscript received: September 5, 2024
Accepted manuscript online: September 13, 2024
Version of record online: ■■, ■■

RESEARCH ARTICLE

RuNi nanoparticles displaying a segregated structure were synthesised in the presence of a phosphine ligand. Spectroscopic techniques confirmed the coordination of the phosphine ligand onto the surface of the nanoparticles. The presence of the phosphorus ligand modified the catalytic performance of the nanomaterials.

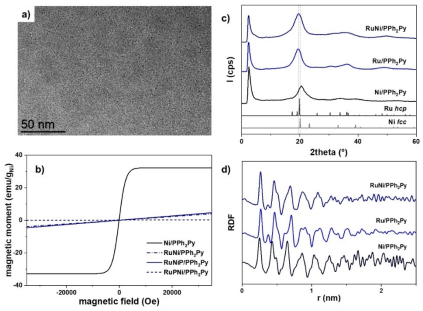

*M. Cardona-Farreny, H. Ishikawa, A. O. Odufejo Ogoe, S. Mallet-Ladeira, Y. Coppel, P. Lecante, J. Esvan, K. Philippot, M. R. Axet**

1 – 11

Colloidal Bimetallic RuNi Particles and their Behaviour in Catalytic Quinoline Hydrogenation